Supporting Information

Reduction of nitric oxide to HNO by sodium dithionite: kinetics and mechanism

Paola Vargas,[a] Mateus F. Venâncio,[b] Willian R. Rocha,[c] Sebastián A. Suarez,[d,*] Fabio A. Doctorovich.[a,*]

[a] Departamento de Química Inorgánica, Analítica, y Química Física, Facultad de Ciencias Exactas y Naturales, Universidad de Buenos Aires, INQUIMAE-CONICET. Ciudad Universitaria, Pab. 2, Piso 3, C1428EHA Buenos Aires, Argentina

[b] Laboratório de Termodinâmica, Espectroscopia e Cinética, LaTEC, Universidade Federal da Bahia, Instituto de Química, Departamento de Físico-Química, Salvador, Bahia, 40170-110, Brazil.

[c] Laboratório de Estudos Computacionais em Sistemas Moleculares, eCsMo[Lab], Departamento de Química – ICEX, Universidade Federal de Minas Gerais, Belo Horizonte, Minas Gerais, 31270-901, Brazil.

[d] Departamento de Química Analítica y Análisis Instrumental. Facultad de Ciencias. c/Francisco Tomás y Valiente, No 7. Campus de Excelencia de la Universidad Autónoma de Madrid, Madrid 28049. Spain.

*sebastian.suarez@uam.es , doctorovich@qi.fcen.uba.ar

16-digit ORCID of the author(s): 0000-0002-9832-6097, 0000-0002-8088-447X, 0000-0002-0025-2158, 0000-0003-0236-5743, 0000-0003-1088-2089

Structure of the porphyrin used as an HNO sensor

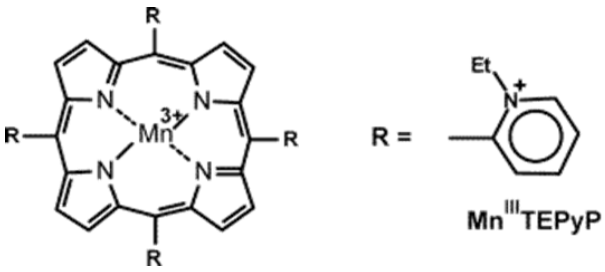

Scheme S1. Structure of manganese(III) meso-tetrakis (N-ethylpyridinium-2-yl) porphyrin (Mn(III)TEPyP).

Attenuated total reflectance Fourier transform infrared (ATR-FTIR) spectroscopy of sulfur molecules

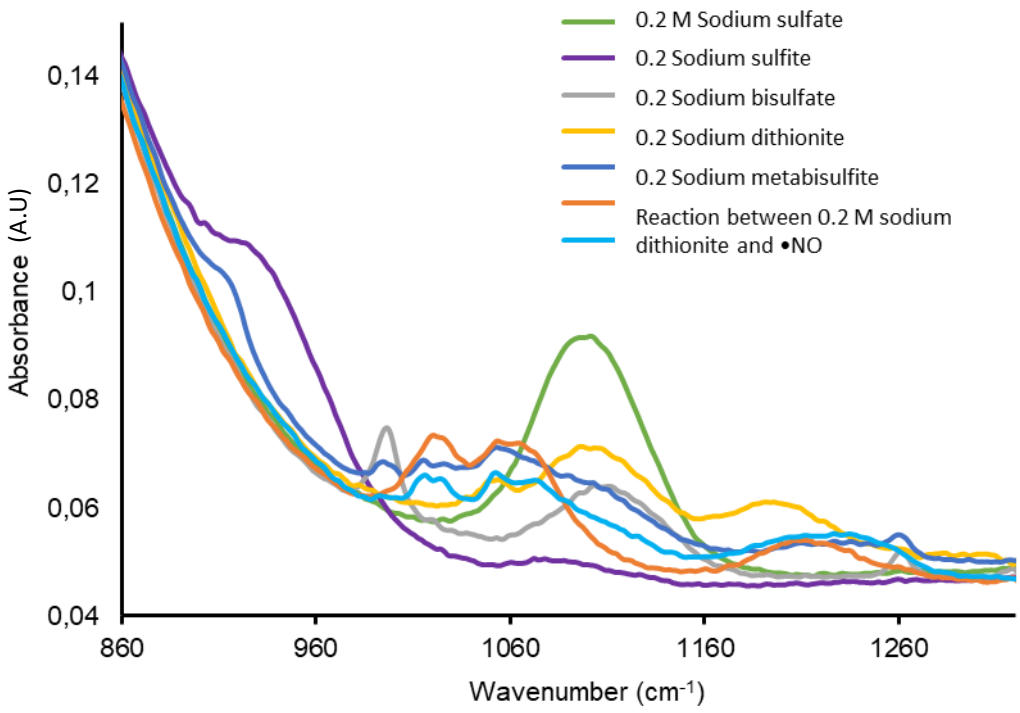

Fig.S1 Comparison between the ATR-FTIR spectra of sodium sulfate, sodium thiosulfate, sodium sulfite, sodium bisulfate, sodium metabisulfite, sodium dithionite, and the reaction between sodium dithionite and NO•.

NO• in excess

As outlined in the manuscript, the kinetics of dithionite consumption were monitored by following its absorbance at 315 nm after the addition of a known volume of a saturated aqueous NO• solution. When NO• was present in excess with respect to dithionite, the initial decrease in absorbance could not be satisfactorily described by simple kinetic models, such as linear or single-exponential functions, even within the first seconds after the reaction onset (**Fig. S2** and **Fig. S3**).

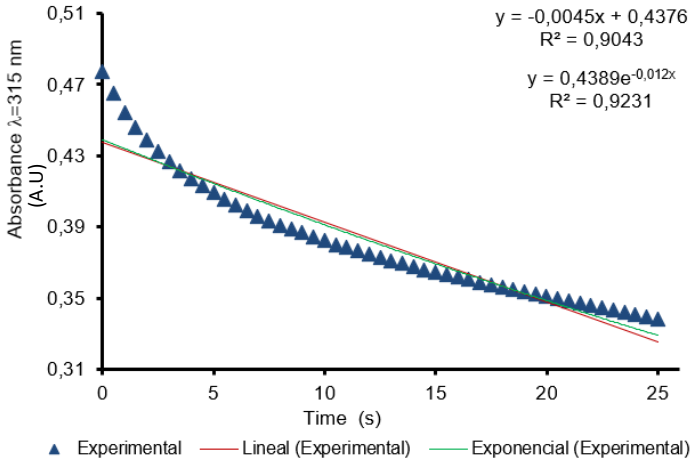

Fig.S2 Linear and exponential fit for the reaction carried out with 35 uM dithionite and 150 uM NO •

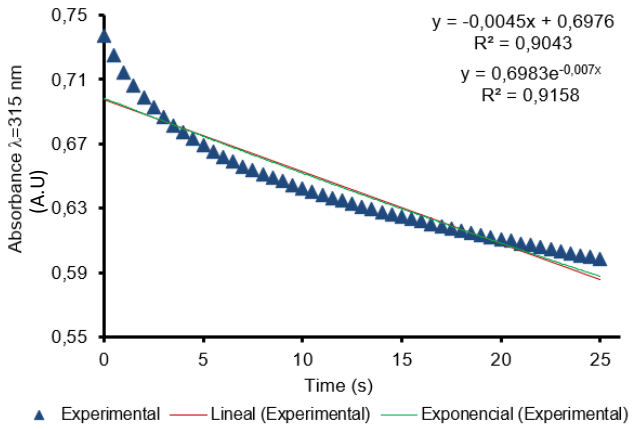

Fig.S3 Linear and exponential fit for the reaction carried out with 60 uM dithionite and 150 uM NO •

Accordingly, the initial portion of the kinetic traces could not be analysed using simple rate laws. To further explore the dependence of the reaction rate on dithionite concentration under conditions of excess NO•, kinetic traces were recorded for different initial concentrations of the reductant. The experimental data were then transformed into reaction rates, expressed as $d[S_2O_4^{2-}]/dt \times 10^{-5}$ M s^{-1}, and plotted as a function of $[S_2O_4^{2-}] \times 10^{-6}$ M (**Fig. S4**).

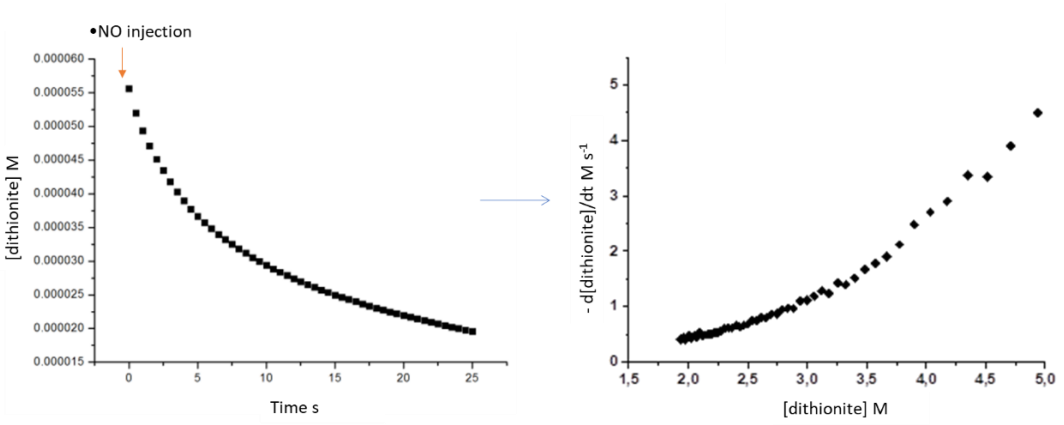

Fig.S4 Example of one of the experimental curves of 60 µM dithionite consumption as a function of time from the addition of 250 µM NO• (left). A concentration-dependent consumption rate curve plotted as -d[dithionite]/dt is shown (right). It was calculated every 0.5 seconds as follows: (final concentration - initial concentration)/0.5 s.

It was found that the experimental data could be satisfactorily described by the empirical expression $Z = A + Bx + Cxy$, where Zcorresponds to the reaction rate, A, B, and C are adjustable parameters, and x and y represent the concentrations of dithionite and NO•, respectively. An example of this analysis is shown in **Fig. S5** for a system containing 60 µM dithionite and 250 µM NO•. In this representation, the fitted parameters account for contributions that either increase or decrease the observed reaction rate, without implying a unique physical meaning at this stage.

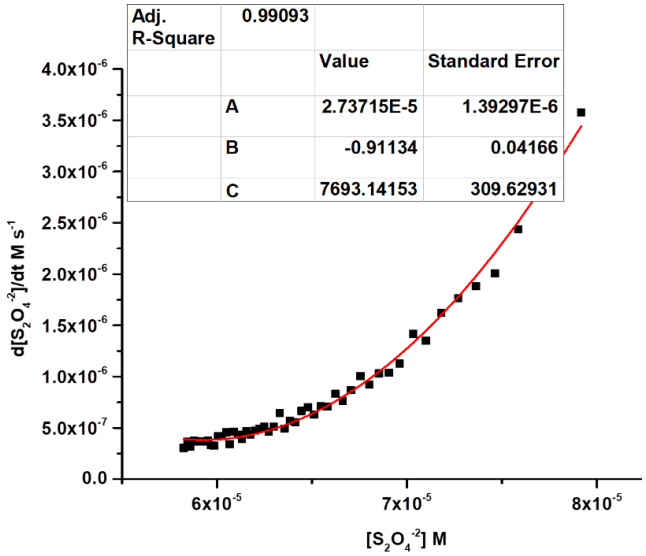

Fig.5 Experimental curve dithionite 60 µM and NO• 250 µM. Experimental data (black squares). Curve constructed from the fit to the equation Z = A + Bx + Cxy (red line).

Therefore, the empirical equation can be expressed as the sum of three contributions: a constant term (A), a term proportional to the dithionite concentration (B·x), and a mixed term proportional to the concentrations of dithionite and NO• (C·x·y). These contributions can be interpreted phenomenologically as accounting for baseline dithionite consumption, concentration-dependent effects, and interactions between dithionite and NO•, respectively. For convenience, the parameters A, B, and C are denoted as k_i, k_r, and $k_d$in the discussion below, without implying a unique mechanistic assignment. When this equation was applied to 12 experimental kinetic traces obtained at different dithionite and NO• concentrations, average values and standard deviations for the fitted parameters were obtained (Table S1).

Table S1. Average values of the kinetic parameters and their respective standard deviations

	Constant consumption (A)	**Concentration-dependent term (B*x)**	**Consumption by NO• (C*x*y)**
Formula	k_i	$k_r[S_2O_4^{2-}]$	$k_d[S_2O_4^{2}][NO•]$
Constant parameter value	(2.9 ± 1.7) x 10^{-5}	-0.9 ± 0.4	8400 ± 1600

A mechanistically compatible reaction network was analysed to rationalize the observed kinetic behaviour. Although the $SO_2•^-$ monomer is generally considered the most reactive species, previous studies have shown that both monomeric and dimeric forms can participate in redox processes, sometimes concurrently. This complexity was incorporated into a reaction framework describing the interaction between dithionite and NO• under anaerobic conditions, particularly when NO• is present in excess relative to dithionite (**Fig. S6**). The experimental observations are consistent with dithionite consumption pathways that involve the transient formation of HNO, leading to N_2O and $HSO_3^-/HS_2O_5^-$ as final products. In addition, recombination processes involving sulfur-centred radicals may partially reform dithionite under specific conditions, although this does not imply net catalytic turnover. To evaluate the thermodynamic accessibility of the individual elementary steps depicted in **Fig. S6**, computational analysis was performed.

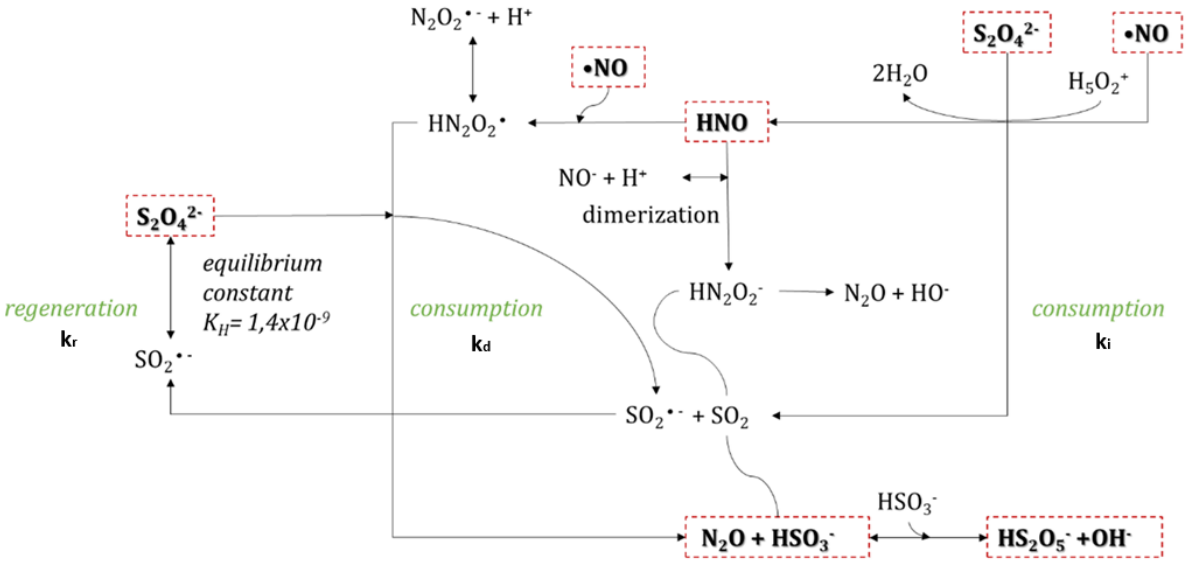

Fig.S6 Network of feasible reaction pathways. In this scheme, k_r accounts for regeneration pathways associated with sulfur-centred radical recombination, k_d captures the ensemble of NO•-dependent consumption pathways, and k_i represents NO•-independent dithionite consumption processes. The assignment reflects phenomenological rate terms rather than individual elementary steps.

Under these conditions, the relative contribution of the different dithionite consumption pathways is expected to depend on the concentrations of dithionite and NO•, consistent with a rate that increases with both reactant concentrations (k_d $[S_2O_4^{2-}]$ [NO•]). This behaviour is captured by the phenomenological rate expression described above. The experimental observations are consistent with reaction pathways involving reduction of NO• and oxidation of dithionite, as supported by the detection of HNO as a transient intermediate (see Eq. S1).

$$S_2O_4^{2-} + H_5O_2^{+} + NO• \rightarrow HNO + SO_2 + SO_2^{•-} + 2H_2O \quad \text{(Eq.S1)}$$

A plausible mechanistic scenario involves initial reduction of NO• leading to the transient formation of HNO, accompanied by oxidation of dithionite to sulfur-centred species such as $SO_2•^-$ and SO_2. In the absence of sulfur reagents, HNO is well known to undergo rapid dimerization to yield N_2O and H_2O. Within the present system, however, additional reaction pathways can be envisaged in which nitrogen–nitrogen bond formation and sulfur redox chemistry are coupled. For example, reaction of HNO-derived species with SO_2 may provide an alternative route to N_2O formation accompanied by

bisulfite production (Eq. S2). Subsequently, the well-established equilibrium between bisulfite and metabisulfite can account for the presence of both species in solution (Eq. S3).

$$cis - HN_2O_2^- + SO_2 \rightarrow N_2O + HSO_3^- + H^+ \quad \text{(Eq.S2)}$$

$$2HSO_3^- \leftrightarrow HS_2O_5^- + OH^- \quad \text{(Eq.S3)}$$

A computational analysis was performed to evaluate the thermodynamic feasibility of individual elementary steps within the proposed reaction network. **Fig. S7** depicts optimized geometries for a representative pathway involving the direct interaction between dithionite and NO•, highlighting the role of two explicit water molecules in facilitating proton transfer and charge redistribution. Although the formation of HNO in this pathway is associated with an endergonic free energy change, subsequent reactions involving HNO are strongly thermodynamically favoured. In particular, **Fig. S8** shows that HNO dimerization is associated with a decrease in standard Gibbs free energy of 54.24 kcal mol^{-1}. This thermodynamic driving force provides a plausible explanation for the effective consumption of HNO once formed, thereby favouring overall progression toward the observed nitrogen-containing end product.

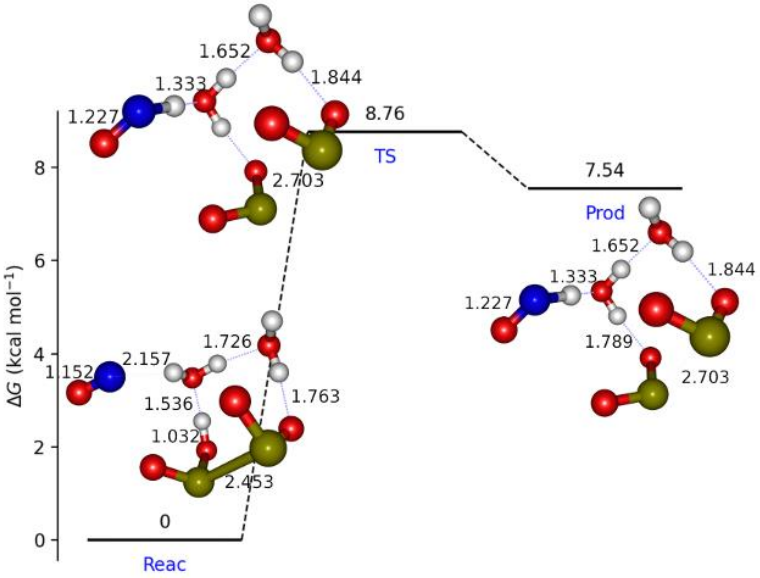

Fig.S7. Reaction free energy profiles in kcal mol^{-1} and optimized geometries for Reac, TS, and Prod for $HS_2O_4^-$ + NO• +2H_2O → HNO + SO_2^- + $SO_2^{\bullet-}$ + H_2O reaction at r^2-SCAN(D4)/Def2-TZVPP(SMD) level of theory.

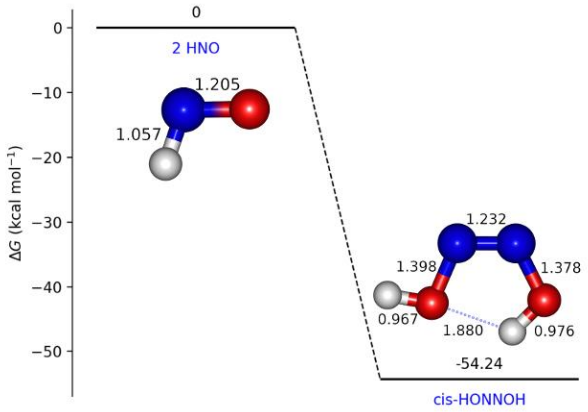

Fig.S8 - Reaction free energy profiles, in kcal mol^{-1}, for HNO dimerization.

It is well established that dimerization of HNO leads initially to the formation of $H_2N_2O_2$. At near-neutral pH, the reported pK_a values of this species (pK_{a1} = 6.9 and pK_{a2} = 11.6) indicate that the mono-deprotonated form, $HN_2O_2^-$, is expected to be predominant under the experimental conditions employed.[77,78] **Fig. S9** shows optimized geometries for a representative reaction pathway involving abstraction of an OH^- group from cis-$HN_2O_2^-$ by SO_2, leading to the formation of HSO_3^- and N_2O (Eq. S2). The corresponding free energy profile for this process is shown in Fig. S10. The calculations indicate that this transformation is thermodynamically favourable, with an overall stabilization of approximately 45 kcal mol^{-1} in Gibbs free energy.

Fig. S9 - Optimized geometries for the proposed mechanism for N_2O formation.

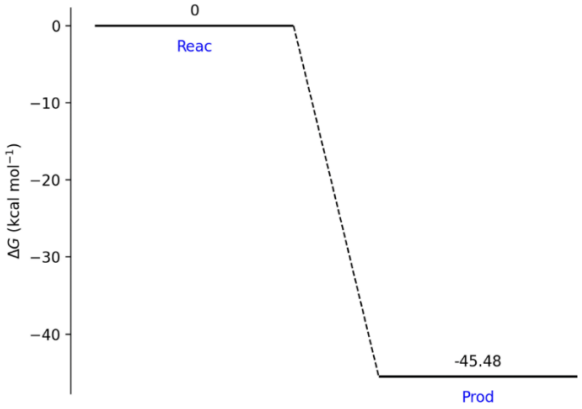

Fig. S10 - Free gibbs energy, in kcal mol^{-1}, for reaction between cis-$HN_2O_2^-$ and SO_2 to yield HSO_3^- and N_2O.

The phenomenological kinetic analysis indicates that the overall reaction rate increases with both dithionite and NO• concentrations. Within this framework, the fitted constant term A may reflect baseline processes that are not directly dependent on reactant concentrations, without implying a unique elementary step. This observation motivated consideration of alternative reaction pathways involving transient radical intermediates. One such pathway reported in the literature involves reaction between HNO and NO• to form the HN_2O_2• radical (Eq. S14), which can subsequently react further with NO• to generate $N_3O_3^-$ and, ultimately, N_2O and NO_2^-.[79] However, no formation of NO_2^- was detected by ion exchange chromatography under the experimental conditions employed, indicating that this pathway does not contribute significantly in the present system. To further assess alternative possibilities, computational calculations were performed to evaluate whether HN_2O_2• could react directly with dithionite. The results indicate that reaction between HN_2O_2• and $S_2O_4^{2-}$ to yield N_2O, SO_2•$^-$ and HSO_3^- (Eq. S15) is thermodynamically accessible. As shown in Fig. **S11**, this transformation involves a modest activation barrier of approximately 10 kcal mol^{-1}, followed by a substantial stabilisation of nearly −50 kcal mol^{-1} in Gibbs free energy. These results support the feasibility of this pathway, without implying that it represents the dominant route under the experimental conditions studied.

$$HNO + NO\bullet \rightarrow HN_2O_2^{\bullet} \qquad \text{(Eq.SI4)}$$

$$HN_2O_2^{\bullet} + S_2O_4^{2-} \xrightarrow{k_i} HSO_3^- + SO_2^{\bullet -} + N_2O \qquad \text{(Eq.SI5)}$$

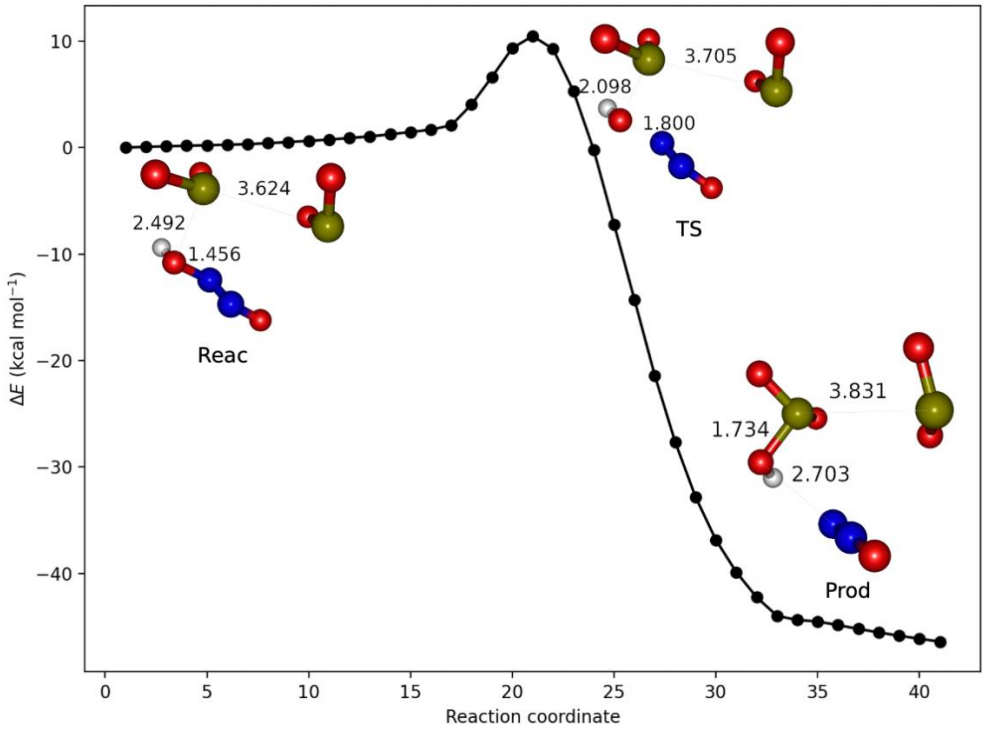

Fig. S11. Optimized geometries and potential energy profile (in kcal mol^{-1}) for a representative reaction between HN_2O_2• and dithionite ($S_2O_4^{2-}$), illustrating a feasible pathway leading to SO_2•$^-$, HSO_3^- and N_2O.

As suggested by the phenomenological kinetic analysis, the fitted rate expression includes a term proportional to the dithionite concentration. This term may reflect the contribution of processes that are not directly linked to the instantaneous NO• concentration, without implying a closed catalytic cycle. As discussed above, SO_2•$^-$ radicals formed during dithionite oxidation can recombine in solution to regenerate $S_2O_4^{2-}$ through a well-established equilibrium (monomerization equilibrium, K_H = 1.4 × 10^{-9}). Since SO_2•$^-$ species are generated as intermediates in multiple consumption pathways, recombination processes may occur concurrently with dithionite consumption. The observed kinetic behaviour is therefore consistent with the simultaneous operation of dithionite consumption and recombination pathways. Computational calculations support the energetic accessibility of these processes, showing modest activation barriers for the formation of transition complexes from the reactants and significant stabilisation upon progression to products (**Fig. S11**). These results indicate that such processes are feasible under the experimental conditions, without implying their dominance or exclusivity.

Reaction performed in deuterium oxide

When a reaction is carried out in deuterium oxide (D_2O), isotopic substitution of H by D can modify the observed kinetics. Solvent kinetic isotope effects (SKIEs) may manifest as changes in rate constants when hydrogen transfer or bond breaking/formation involving hydrogen occurs in, or near, the rate-determining step.[80] In the system studied here, the kinetics observed when D_2O was used instead of H_2O (with the pH adjusted to 7.25 using the appropriate correction) showed an increase in the effective rate of dithionite consumption by NO• (see **Fig. 6** in the MS). This behaviour corresponds to an inverse solvent isotope effect. Unlike normal isotope effects, which may arise from SKIEs, solvent equilibrium isotope effects (SEIEs), or a combination of both, inverse isotope effects are most commonly dominated by SEIEs, that is, by equilibria that are thermodynamically more favourable in D_2O.[80]

Under the experimental conditions employed, the concentrations of protonated dithionite species are expected to be very low. The reported pK_a values for the protonated forms of dithionite, $H_2S_2O_4$ and $HS_2O_4^-$, are pK_{a1} = 0.35 and pK_{a2} = 2.45, respectively.[81] In addition, D_2O has a lower ionic product constant (K_w = 8.9 × 10^{-16} at 20 °C) than H_2O.[82] These considerations make it unlikely that the observed isotope effect arises from direct hydrogen transfer in the rate-determining step. On the other hand, formation of the SO_2•$^-$ radical occurs as an intermediate in the reaction system. In this context, the observed

solvent-dependent rate enhancement may be associated with differential stabilisation of this radical species in D_2O relative to H_2O. Since the electronic structure is identical for hydrogen and deuterium, isotope effects arise from differences in atomic mass and the corresponding zero-point vibrational energies. Heavier isotopes lead to lower vibrational frequencies and lower zero-point energies.[83] As a consequence, hydrogen bonds involving D_2O are generally stronger than those involving H_2O.[84] Accordingly, it can be proposed that interactions between $SO_2\bullet^-$ and the solvent via deuterium bridging are stronger in D_2O than the corresponding interactions mediated by H_2O, potentially contributing to stabilisation of this intermediate.

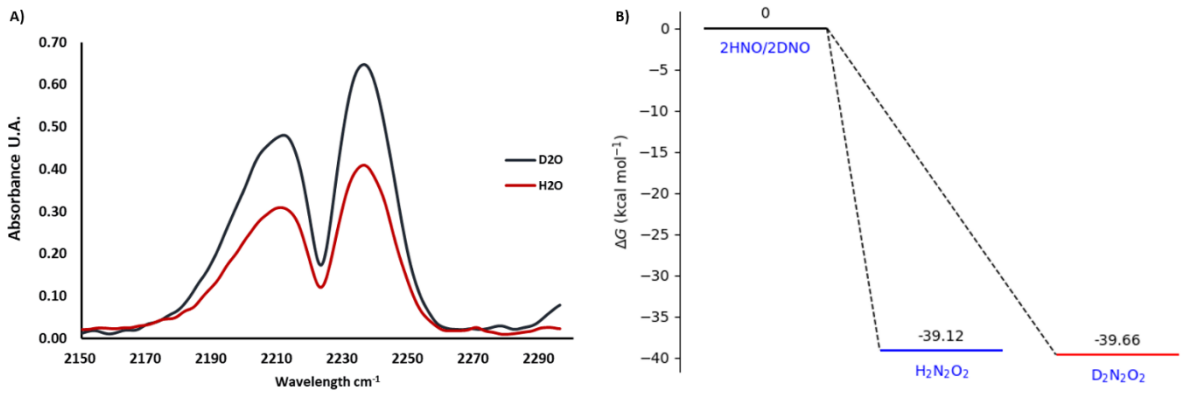

Fig. S12. A) N_2O formation measured by headspace IR for the reaction between dithionite and NO• carried out in H_2O and D_2O (30 minutes). The increased N_2O signal in D_2O indicates an inverse solvent isotope effect on N_2O formation ($H_2O/D_2O \approx 0.62$)**. B)** Free Gibbs energy change (ΔG, kcal·mol^{-1}) for the dimerization of HNO and DNO to form hyponitrous acid isotopologues (2 HNO → $H_2N_2O_2$ and 2 DNO → $D_2N_2O_2$). The calculated ΔG values are very similar for both processes, indicating only a minor energetic isotope effect for HNO/DNO dimerization under the present computational model.

Anaerobic decomposition of 172 µM dithionite at pH 7.4 (10 mM) and room temperature:

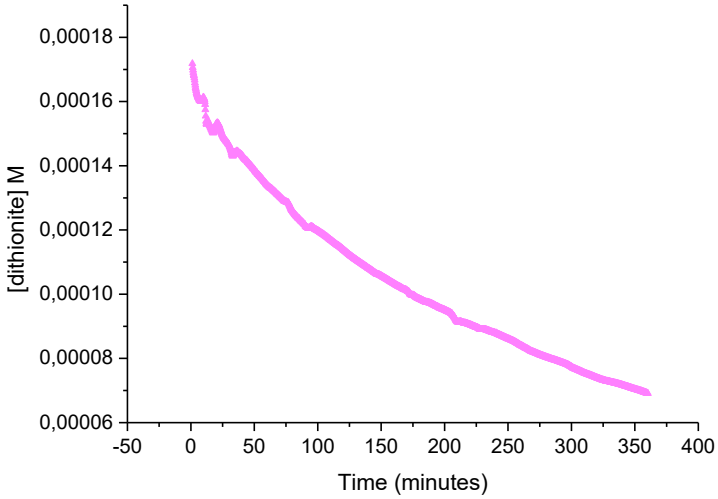

Fig.S13 - The anaerobic decomposition of dithionite was measured by UV-visible, taking a spectra every 15 seconds for 6 hours. Concentrations were calculated from the absorbance peak at 315 nm and the molar extinction coefficient of 8000 M^{-1} cm^{-1}.

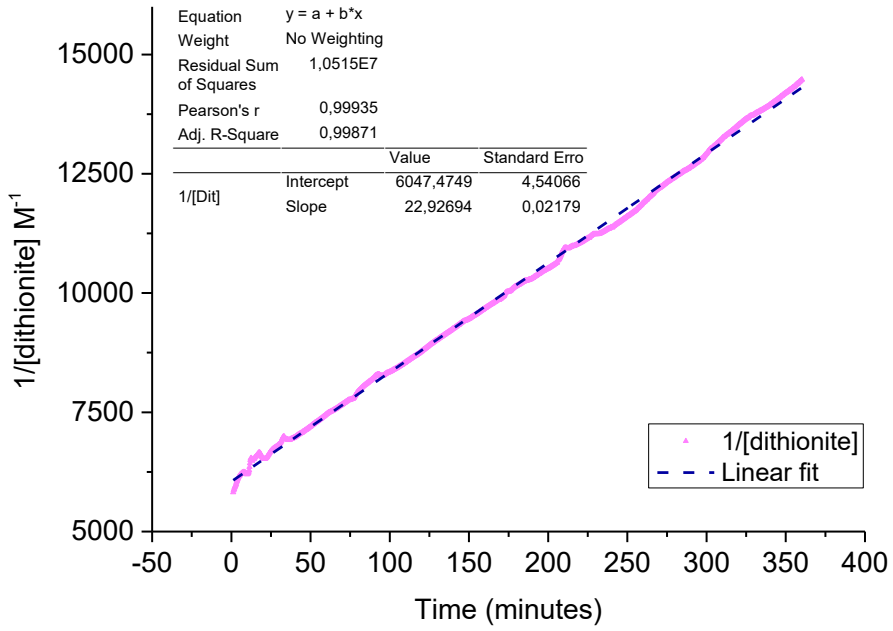

Fig.S14 - Linear regression of 1/[dithionite] as a function of time. The value of the slope of this line corresponds to the reaction constant for a second order reaction.

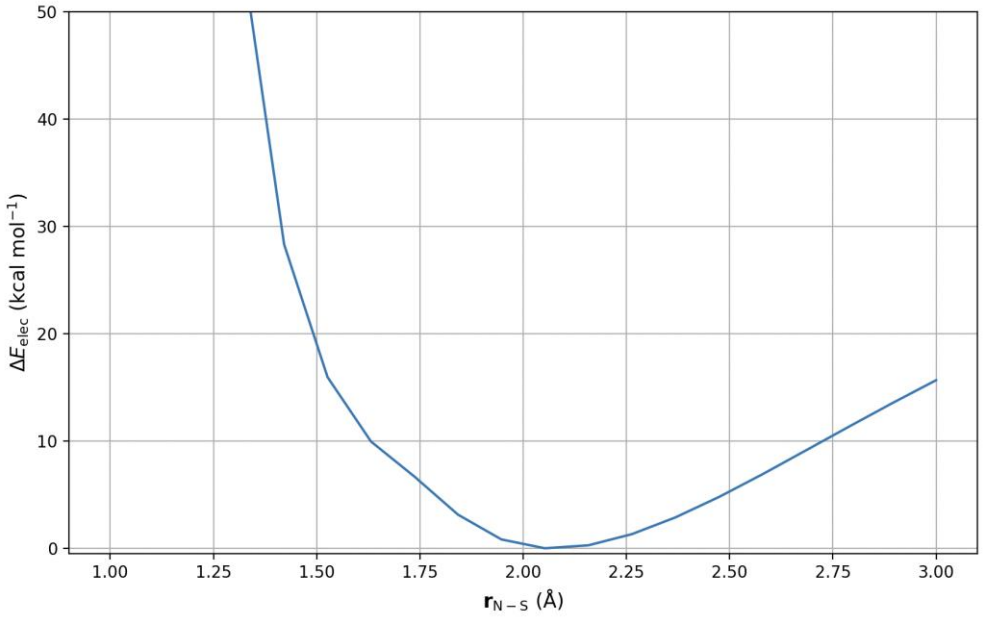

Fig.S15 - One-dimensional electronic energy profile along the N–S coordinate for the interaction between NO• and SO_2•⁻. The calculated energy decreases by approximately 15 kcal·mol⁻¹ as the distance is reduced from 3.0 to 2.1 Å, indicating the favorable formation of a stabilized intermediate adduct.

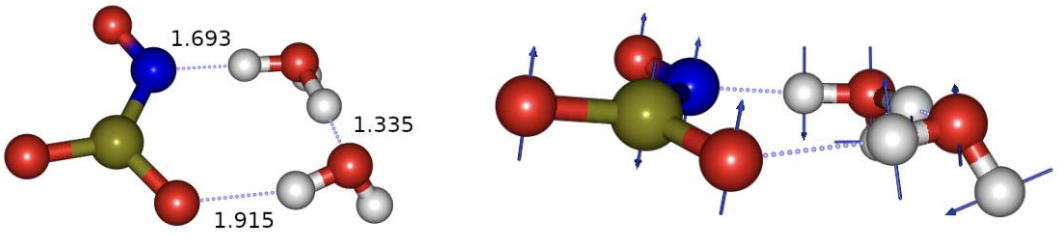

Fig.S16 - Left: Optimized transition state structure for the protonation of the SO_2NO^- intermediate by a Zundel ion ($H_5O_2^+$), highlighting the hydrogen-bonding network involved in the proton transfer process. **Right**: Displacement vectors corresponding to the imaginary frequency (i286.48 cm^{-1}) of the transition state, showing that the vibrational mode is associated with structural reorganization of the $SO_2NO^-\cdot 2H_2O$ adduct rather than HNO formation.

SI references

77 N. N. Greenwood and A. Earnshaw, *Chemistry of the Elements*, 2nd edn., 1997.
78 J. E. House and K. A. House, *Descriptive Inorganic Chemistry*, 3rd edn., Elsevier, 2016.
79 S. V. Lymar, V. Shafirovich and G. A. Poskrebyshev, *Inorg. Chem.*, 2005, **44**, 5212–5221.
80 P. L. Fernandez and A. S. Murkin, *Molecules*, 2020, **25**, 1933.
81 C. E. Housecroft and A. G. Sharpe, *Inorganic Chemistry*, 4th edn., 2012.
82 J. Katz, *Am. Sci.*, 1960, **48**, 544–580.
83 L. J. Altman, P. Laungani, G. Gunnarsson, H. Wennerström and S. Forsén, *J. Am. Chem. Soc.*, 1978, **100**, 8264–8266.
84 S. Scheiner and M. Čuma, *J. Am. Chem. Soc.*, 1996, **118**, 1511–1521.